Backbone NMR Assignments and H/D Exchange Studies on the Ferric Azide- and Cyanide-Inhibited Forms of *Pseudomonas aeruginosa* Heme Oxygenase[†,‡]

Juan Carlos Rodríguez,[§] Angela Wilks,[||] and Mario Rivera*[,§]

Department of Chemistry, The University of Kansas, Multidisciplinary Research Building, 2030 Becker Drive, Lawrence, Kansas 66047, and Department of Pharmaceutical Sciences, School of Pharmacy, University of Maryland, Baltimore, Maryland 21201-1180

Received January 4, 2006; Revised Manuscript Received February 16, 2006

ABSTRACT: The 198 amino acid long heme oxygenase from *Pseudomonas aeruginosa* (*pa*-HO) was studied by multinuclear and multidimensional NMR spectroscopy in its paramagnetic cyanide-inhibited (*pa*-HO−CN) and azide-inhibited (*pa*-HO−N_3) forms. Nearly complete backbone assignments (>93%) of all non-proline residues have been obtained, with the majority of the nonassigned residues corresponding to the first 10 amino terminal residues. Resonances strongly affected by heme iron paramagnetism were assigned with the aid of selective amino acid labeling and experiments tailored to detect fast relaxing signals, whereas the rest of the polypeptide was assigned using conventional three-dimensional NMR experiments. Amide chemical shift assignments were used to monitor the rate of exchange of backbone protons in hydrogen−deuterium exchange experiments. The polypeptide in the *pa*-HO−N_3 complex was found to be significantly less prone to exchange than the polypeptide in *pa*-HO−CN, which we interpret to indicate that *pa*-HO−N_3 is conformationally less flexible than *pa*-HO−CN. The differences in protection factors extend to regions of the protein remote from the heme iron and distal ligand. Mapping the differences in protection factors into the X-ray crystal structure of *pa*-HO [Friedman, J., Lad, L., Li, H., Wilks, A. Poulos, T. L. (2004) *Biochemistry 43,* 5239−5345] suggests that the distinct chemical properties imparted by the coordination of azide or cyanide to the heme iron [Zeng, Y. Caignan, G. A., Bunce, R. A., Rodríguez, J. C., Wilks, A., Rivera, M. (2005) *J. Am. Chem. Soc. 127,* 9794−9807] are transmitted to the polypeptide by a network of structural water molecules extending from the active site to the surface of the enzyme. Finally, while the ^{1}H amide resonance of Gly125 was too broad to detect, the corresponding ^{15}N resonance exhibits a large downfield shift, large line width, steep temperature dependence, and a larger than usual upfield deuterium isotope effect. These properties indicate unpaired spin delocalization from the heme iron into the Gly ^{15}N atom via formation of a hydrogen bond between the coordinated azide nitrogen and the Gly125 N−H.

Heme oxygenase (HO)[1] catalyzes the degradation of heme to iron, biliverdin, and carbon monoxide (*1*). In mammals, the release of iron from heme is very important for iron recycling because less than 4% of daily requirements are absorbed from dietary intake (*2*). The biliverdin−bilirubin redox couple act as powerful antioxidants (*3*−*5*), and CO has been implicated as a neural messenger and modulator of vascular tone (*6*). Heme oxygenase has also been identified in pathogenic bacteria (*7*−*13*), suggesting that bacterial HOs are an integral part of an efficient machinery for the mining of heme iron from mammalian hosts. The first bacterial heme oxygenase to be characterized by biophysical methods is the enzyme from *Corynebacterium diphtheriae* (*7*, *14*, *15*). Shortly thereafter, detailed biophysical characterizations were reported for heme oxygenase enzymes from *Neisseria meningitidis* (*16*, *17*) and from *Pseudomonas aeruginosa* (*18*, *19*). *P. aeruginosa* is an opportunistic pathogen capable of infecting burn victims and patients with cystic fibrosis, emphysema, and cancer, and in these cases, it presents a difficult challenge to treatment and eradication. Infections with *P. aeruginosa* are often persistent because of the development of multiple drug resistance and the formation of biofilms (*20*). Although pseudomonads produce and secrete extremely efficient siderophores, they can also utilize heme and heme-proteins as sole sources of iron (*21*, *22*). In fact, mutants where the *pigA* gene, which codes for a heme oxygenase (*pa*-HO), has been knocked out are unable to use heme as a source of iron (*10*).

The catalytic cycle of heme breakdown (Scheme 1) is similar in mammalian and bacterial heme oxygenase en-

[†] This work was supported by NIH Grant GM 50503 to M.R.

[‡] NMR backbone assignments for the azide- and cyanide-inhibited forms of *Pseudomonas aeruginosa* heme−heme oxygenase have been deposited at the BioMagResBank under accession numbers 6983 and 6987, respectively.

* To whom correspondence should be addressed at Department of Chemistry, The University of Kansas, Multidisciplinary Research Building, 2030 Becker Drive, Lawrence, KS 66047. Phone: 785-864-4936. Fax: 785-864-5396. E-mail: mrivera@ku.edu.

[§] The University of Kansas.

[||] University of Maryland.

[1] Abbreviations: DSS, dimethylsilapentane-5-sulfonic acid; HO, heme oxygenase; IPTG, isopropyl-β-D-thiogalactopyranoside; NMR, nuclear magnetic resonance; *pa*-HO, *Pseudomonas aeruginosa* heme oxygenase; *pa*-HO−N_3, azide-inhibited form of *pa*-HO; *pa*-HO−CN, cyanide-inhibited form of *pa*-HO; *pig*A, *Pseudomonas* iron-regulated gene A.

10.1021/bi0600188 CCC: $33.50
Published on Web 03/16/2006

Scheme 1

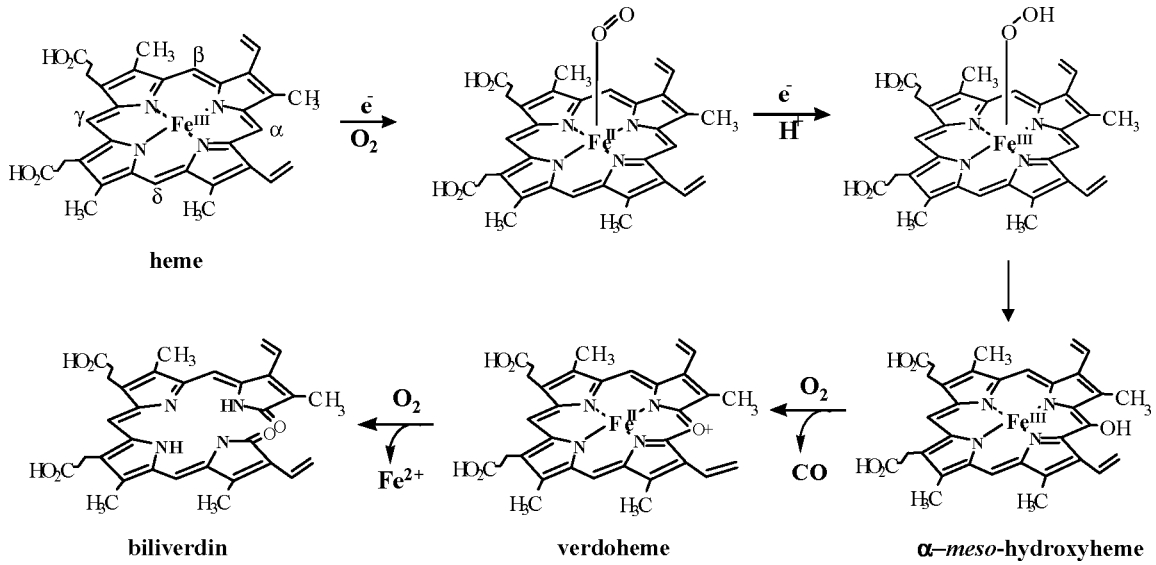

zymes. Moreover, heme oxygenase and monooxygenase enzymes share a similar mechanism of O_2 activation, which leads to the formation of a ferric hydroperoxide intermediate (Fe^{III}−OOH) (*23*−*25*). However, once formed, the Fe^{III}−OOH intermediate can follow two divergent paths: (a) the formation of an oxoferryl species, thus, avoiding the hydroxylation of heme (*26*) or (b) the efficient reaction with the porphyrin macrocycle to produce *meso*-hydroxyheme. Consequently, the study of structural and dynamic properties that accelerate heme hydroxylation in HO is an important aspect of generating a comprehensive understanding of O_2 activation at heme centers (*26*−*28*).

Studies conducted with model complexes of the Fe^{III}−OOH intermediate (*29*) and with the hydroxide (*30*) and azide (*31*) complexes of *pa*-HO led us to suggest that coordination of HOO^- in the distal site of HO promotes heme electronic structures that enhance the reactivity of the heme so that it actively participates in its own hydroxylation. Hence, when Fe^{III}−tetraphenylporphyrin was axially coordinated by a methoxy and an alkylhydroperoxy ligand, or by two alkylhydroperoxy ligands, the resultant complex was found to be in thermal equilibrium between a ruffled porphyrin with an $S = 1/2$, $(d_{xz}, d_{yz})^4(d_{xy})^1$ electron configuration ($(d_{xy})^1$ hereafter) and a planar porphyrin with the more common $S = 1/2$, $(d_{xy})^2(d_{xz},d_{yz})^3$ electron configuration (d_π hereafter). The population with the former electron configuration was predicted to be the predominant species at ambient temperature (*29*). The fact that low-spin ferrihemes with an unpaired electron in the d_{xy} orbital place a significant amount of spin density at the meso carbons (*32*) led us to propose a radical mechanism for meso-carbon hydroxylation (*28*, *29*). In subsequent studies, the hydroxide and azide complexes of *pa*-HO (*pa*-HO−OH and *pa*-HO−N_3, respectively) were investigated at ambient temperatures as models of the ferric hydroperoxide intermediate. Results from these investigations indicated that the nature of the distal ligand largely influences the electronic structure and conformation of the heme in HO (*28*). Thus, when OH^- serves as the distal ligand, the heme in *pa*-HO−OH adopts at least three populations with distinct electronic structures, two of these, $(d_{xy})^1$ and $S = 3/2$, $(d_{xy})^2(d_{xz},d_{yz})^2(d_z^2)^1$, place significant spin density at the meso positions (*30*). Azide has a ligand field strength somewhat larger than OH^- (*33*), and the *pa*-HO−N_3 complex exists as an equilibrium of two populations, one with an $S = 1/2$, d_π electron configuration and planar heme and the second with an $S = 3/2$, $(d_{xz},d_{yz})^3(d_{xy})^1(d_z^2)^1$ spin state and nonplanar heme (*31*). In contrast, coordination of CN^- (higher field strength than OH^- or N_3^-), which is not capable of accepting a proton to form a hydrogen bond at the coordinated carbon atom, results in a complex with the common $S = 1/2$, d_π electron configuration and planar porphyrinate (*34*).

Scheme 2

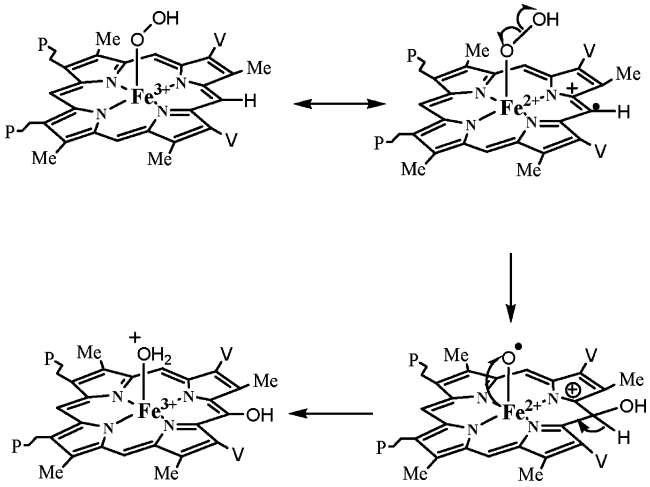

These findings led us to suggest that if the field strength of the HOO^- ligand is similar to that of the OH^-, the nonplanar deformations and unpaired spin density at the meso carbons that are characteristic of populations with the $(d_{xy})^1$ and $S = 3/2$ spin states would facilitate homolytic cleavage of the O−O bond by efficiently trapping the ·OH radical at an sterically unprotected meso carbon (Scheme 2) (*18*, *28*, *29*, *31*). In this context, it is interesting that results from theoretical studies have suggested that heme hydroxylation is more likely to occur via a stepwise mechanism in which homolytic cleavage of the O−O bond is followed by trapping of the ·OH radical by the porphyrin. In addition, the calculations also suggest that homolytic cleavage of the O−O bond proceeds via a species with an electronic structure resembling a $Por^{+\bullet}Fe^{III}OH$−HO· (*35*). Hence, notions derived

independently from spectroscopic and from theoretical investigations are in good agreement.

Heme electronic structures that place a significant amount of unpaired spin density at the meso carbons in *pa*-HO have been attained upon coordination of sixth ligands capable of accepting a proton to form a hydrogen bond at the coordinating atom, that is, OH^-, or N_3^-, and presumably HOO^-. In this context, it is interesting that the crystal structure of the azide complex of rat HO-1 indicates a hydrogen bond between conserved Gly143 NH and the coordinating nitrogen of the azide ligand (*36*). The equivalent residue in *pa*-HO is Gly125, which we hypothesized may donate a proton to form a hydrogen bond with the coordinated atom of the distal ligand in *pa*-HO−OH and *pa*-HO−N_3, thus lowering its field strength and promoting the unusual heme electronic structures observed with these complexes (*28*). Given that the heme electronic structures of *pa*-HO−OH and *pa*-HO−N_3 suggest them as good models for the elusive Fe^{III}−OOH intermediate, we took advantage of the fact that *pa*-HO−N_3 can be studied at neutral pH to extend our NMR spectroscopic investigations from the heme center to the polypeptide. In addition, because *pa*-HO−CN exhibits the unreactive $S = 1/2$, d_π heme electronic structure (*18*, *31*), we also investigated this complex with the aim of comparing the effects of distinct heme electronic structures on polypeptide properties.

NMR studies on HO from mammalian or bacterial sources have been approached thus far using primarily homonuclear methods, which rely on the larger than normal dispersion of ^{1}H resonances occurring as a result of the hyperfine shift. La Mar and co-workers have used this strategy to produce considerable insight into the architecture of the active site of heme oxygenases (*37*−*39*). To gain a deeper understanding of the structure and dynamics of these enzymes, however, it is important to obtain heteronuclear assignments that permit global probing of the enzyme. As a first effort toward this goal, we report here on the backbone amide resonance assignments of *pa*-HO in complex with azide and cyanide. These assignments were obtained with the aid of homonuclear and heteronuclear 1D-3D NMR experiments applied to uniformly and amino acid-selective isotopically labeled enzyme. With the exception of the work carried out on human heme oxygenase (HO-1) (*37*), there has been no other study reporting on the assignments of backbone amide resonances in heme oxygenase. Hence, the backbone NMR assignments reported here for *pa*-HO−N_3 and *pa*-HO−CN constitute the first example of an HO enzyme for which extensive assignments are available. These assignments, together with the hydrogen−deuterium exchange studies reported herein, represent a first step toward a complete structural and dynamic characterization of the enzyme in solution.

EXPERIMENTAL PROCEDURES

Protein Expression and Purification. The plasmid pET-21a harboring the gene coding for *pa*-HO was transformed into *Escherichia coli* BL21(DE3)-gold cells as described previously (*18*). Five milliliters cultures of the transformed cells were grown overnight at 37 °C in LB medium containing ampicillin (1 mg/L) and used to inoculate 100 mL of fresh LB medium the following morning. The 100 mL culture was incubated at 37 °C to an OD_{600} of 0.5 before a 25 mL aliquot was withdrawn to inoculate 1 L of sterile minimal medium containing nutrients at natural isotopic abundance. These cells were incubated at 37 °C to an OD_{600} of ~0.6 before transferring the culture to centrifuge bottles and spinning them at 3860*g*. The supernatant was discarded, and the cells were resuspended in a small volume of minimal medium containing either 1 g of $^{15}NH_4Cl$ for producing [U-^{15}N]-*pa*-HO, or both 1 g of $^{15}NH_4Cl$ and 2 g of $^{13}C_6$-D-glucose for obtaining [U-^{13}C, U-^{15}N]-*pa*-HO. The cells were then transferred to 1 L of labeled media and incubated at 30 °C to an OD_{600} of 0.7, followed by inducing polypeptide synthesis by addition of IPTG to a final concentration of 1 mM. Incubation was continued for 4−5 h, and the cells were harvested by centrifugation. Cell lysis, purification of the apo-protein, and purification of *pa*-HO reconstituted with hemin were carried out as reported previously (*18*).

Selective amino acid labeling of *pa*-HO was carried out following the protocol reported by Markley and co-workers (*40*) using synthetic rich medium with minor modifications. In brief, the minimal medium used to obtain uniformly labeled protein was supplemented with the following amino acids (g/L): L-Ala (0.5), L-Arg (0.4), L-Asp (0.4), L-Asn (0.4), L-Cys (0.05), L-Gln(0.4), L-Glu (0.65), Gly (0.55), L-His (0.1), L-Ile (0.23), L-Leu (0.23), L-Lys hydrochloride (0.42), L-Met (0.25), L-Phe (0.13), L-Pro (0.1), L-Ser (2.10), L-Thr (0.23), L-Tyr (0.17), L-Val (0.23), and L-Trp (0.05). All amino acids, except L-Trp and the ^{15}N-enriched amino acid were added in solid form to the media prior to autoclaving. The remaining media components, except the ^{15}N-labeled amino acid, were filter-sterilized and added prior to inoculation. For the preparation of [^{15}N-Leu]-*pa*-HO, 5 mL of LB medium was inoculated with the aforementioned *E. coli* cells and grown overnight at 37 °C. The resultant culture was diluted with 100 mL of fresh LB medium, from which 25 mL were aliquoted when the OD_{600} reached 0.5. This aliquot was used to inoculate 1 L of unlabeled minimal medium. The cell suspension was incubated at 37 °C to an OD_{600} of 0.6, at which time the cells were centrifuged as outlined above. The cells were then resuspended in 1 L of synthetic rich medium devoid of L-Leu, and the mixture was incubated at 30 °C to an OD_{600} of 0.7, followed by addition of 0.23 g of ^{15}N-L-Leu together with IPTG (final concentration of 1 mM) and additional 5 h of incubation at 30 °C. Cell harvesting, lysis, and enzyme purification were carried out as described previously (*18*).

Preparation of [^{15}N-Ala]-*pa*-HO was carried out as follows. Five milliliters of LB medium was inoculated with *E. coli* cells as described above. The culture was grown overnight at 37 °C and diluted the next morning with 1 L of synthetic rich medium containing all amino acids except L-Ala. The resultant culture was incubated at 37 °C to an OD_{600} of 0.7, followed by addition of 40 mg of ^{15}N-L-Ala and 1 mL of 1 M IPTG. Cells were harvested by centrifugation following a 5 h incubation period at 30 °C. Lysis and purification were carried out as described previously (*18*).

pa-HO labeled with ^{15}N-Gly was prepared using a procedure similar to that described for [^{15}N-Ala]-*pa*-HO, except that the composition of the medium was altered as follows: 3 g instead of 2 g of glucose was used, and glycine, but not L-Ala, was omitted from the mix. Furthermore, it was necessary to supplement the medium with 2.1 g of L-Ser,

which was added together with 55 mg of ^{15}N-Gly upon inducing with IPTG (final concentration 1 mM). Supplementing the medium with L-Ser during production of [^{15}N-Gly]-*pa*-HO, which effectively doubled the concentration of L-Ser used for labeling *pa*-HO with ^{15}N-Leu and ^{15}N-Ala, was necessary to avoid incorporation of the ^{15}N label into serine residues. Proteins labeled with ^{15}N-Ser in addition to ^{15}N-Gly were consistently obtained when the unmodified medium was used, as determined from the appearance of HSQC cross-peaks attributed to Ser residues (Figure S1, Supporting Information, top spectrum). In contrast, proteins labeled with ^{15}N-Gly and undetectable levels of ^{15}N-Ser incorporation were obtained when the concentration of unlabeled L-Ser in the medium was doubled (Figure S1, Supporting Information, bottom spectrum).

NMR Sample Preparation. Pa-HO−N_3 and *pa*-HO−CN complexes were prepared by adding the appropriate volume of a 1 M NaN_3 or 1 M NaCN stock solution to a solution of *pa*-HO to achieve a 10-fold excess concentration of ligand relative to the concentration of *pa*-HO in solution. Protein concentrations were determined by measuring the absorption of *pa*-HO solutions at 405 nm ($\epsilon_{405} = 129$ mM^{-1} cm^{-1}) (*18*). NMR samples were prepared by adding the appropriate volume of ligand stock solution to a 1.5 mL conical tube containing 450 μL of *pa*-HO and adjusting the pH to 7.0 by addition of microliters amounts of 1 M HCl. NMR samples typically contained 0.7−8 mM *pa*-HO, 7−80 mM NaN_3 or NaCN, and 5−10% D_2O in 50 mM sodium phosphate buffer. Experimental conditions used for specific NMR experiments appear in the corresponding figure captions.

NMR Spectroscopy. NMR experiments used to carry out the backbone assignments were carried out at 32 °C. Two- and three-dimensional NMR experiments (^{1}H-^{15}N-HSQC, ^{1}H-^{15}N-TROSY−HSQC, HNCA, HN(CO)CA, HNCACB, CBCA(CO)NH, (HCA)CONH) were carried out with the aid of a Varian Unity Inova 600 NMR spectrometer equipped with a triple resonance triple-axis gradient probe. Three-dimensional ^{15}N-separated NOESY−HSQC (60 ms mixing time) was obtained at 298 K in a Bruker Avance 800 spectrometer equipped with a 5 mm TXI ^{1}H-^{13}C/^{15}N/D xyz-gradient probe. One-dimensional ^{15}N spectra were collected using a Varian Unity Inova spectrometer equipped with a 5 mm broadband probe and operating at a frequency of 60.781 MHz. All ^{15}N direct detection experiments were collected using a simple delay-90°-acquisition pulse sequence. ^{1}H decoupling was not employed, while fast pulse repetition rates (100 ms acquisition time and 100 ms relaxation delay) were used throughout to achieve saturation of the more slowly relaxing diamagnetic signals. A minimum of 230 000 scans were acquired over a 21.4 kHz spectral width. Specific details of data collection are provided in the corresponding figure captions.

NMR Data Processing and Analysis. Two- and three-dimensional NMR spectra were processed using NMRPipe (*41*) and analyzed with Sparky (*42*). One-dimensional ^{15}N spectra were processed and analyzed with vnmrJ. All one-dimensional ^{15}N spectra exhibited considerable baseline distortion which was alleviated by performing baseline correction on the transformed data. Prior to Fourier transformation, a 10 Hz line broadening apodization was applied to each ^{15}N spectrum. ^{1}H chemical shifts in every spectrum (1D-3D) were referenced to the proton resonance of DSS at 0 ppm, while ^{15}N and ^{13}C shifts were referenced indirectly using the ratios 0.101329118 and 0.251449530, respectively (*43*).

H/D Exchange Studies. Amide hydrogen−deuterium exchange experiments were carried out on 2.4 mM samples of [U-^{15}N]-*pa*-HO−N_3 and [U-^{15}N]-*pa*-HO−CN complexes prepared as described above. The aqueous solvent was eliminated by lyophilization with the aid of a Savant SpeedVac apparatus. Preliminary experiments revealed that portions of the N_3^- and CN^- ligands present in solution are lost due to volatilization during the freeze-drying process. To compensate for this loss, volumes of the NaN_3 and NaCN stock solutions equal to those used for preparing the complexes were added upon redissolving the solid in D_2O (see below). Samples prepared in this fashion exhibited identical NMR and UV−vis spectroscopic characteristics to those shown by the samples prior to lyophilization. Progress of the exchange process was followed by collecting a series of successive 2D HSQC spectra beginning immediately after the solid was redissolved in D_2O. The dead time was approximately 10 min, and spectra were taken at 20 min intervals for the first 7−12 h, and every hour thereafter for a total of 26 h. Each spectrum was acquired at 305 K using the Bruker Avance 800 NMR spectrometer described above. Fast ^{1}H-^{15}N-HSQC spectra (*44*) were collected over a 19.2 kHz (^{1}H) and 3 kHz (^{15}N) spectral widths, with 16 scans per increment and 2560 and 256 complex points for the ^{1}H- and ^{15}N-dimension, respectively. States-TPPI quadrature detection of the ^{15}N nucleus was used. Data were processed using linear prediction to double the number of ^{15}N points and zero-filled in both dimensions to yield a matrix of 1024 (^{15}N) × 4096 (^{1}H). The FID was apodized in both dimensions by application of a 90°-shifted, squared sine bell function. Determination of experimental per residue (k_{ex}) H/D exchange rate constants was carried out as described previously (*45*) by fitting the time-dependent decay of peak intensities to a three-parameter, single-exponential decay function using Sigma Plot 2001, v.7.0. Rate constants were then extracted from the fitting results and subsequently used to calculate residue-specific protection factors as reported by Englander et al. (*46*, *47*). Values for sequence-specific intrinsic rate constants (k_{ch}) were calculated using the spread sheet available from S. Englander's Web site at http://hx2.med.upenn.edu/download.html. Protection factors were determined from the relation $P = k_{ch}/k_{ex}$, where P is the protection factor, and k_{ex} and k_{ch} are as defined above (*46*, *47*). The pH values employed in the calculations were 7.67 and 7.35 for the *pa*-HO−N_3 and *pa*-HO−CN complexes, respectively, which correspond to values read directly from the meter at the end of the H/D exchange experiments.

RESULTS

Assignment of Diamagnetic Amide Backbone Resonances. The ^{1}H-^{15}N HSQC spectra of *pa*-HO−CN and *pa*-HO−N_3 are shown in Figure 1. The signal dispersion and intensity of cross-peaks present in each spectrum are similar to one another and are indicative of the good-quality samples obtained with either ligand. Spectra of similar appearance were obtained at temperatures ranging from 5 to 37 °C with solutions containing between 0.7 and 8 mM protein concentrations. Conventional homonuclear and heteronuclear 2D and 3D NMR experiments were sufficient to assign the

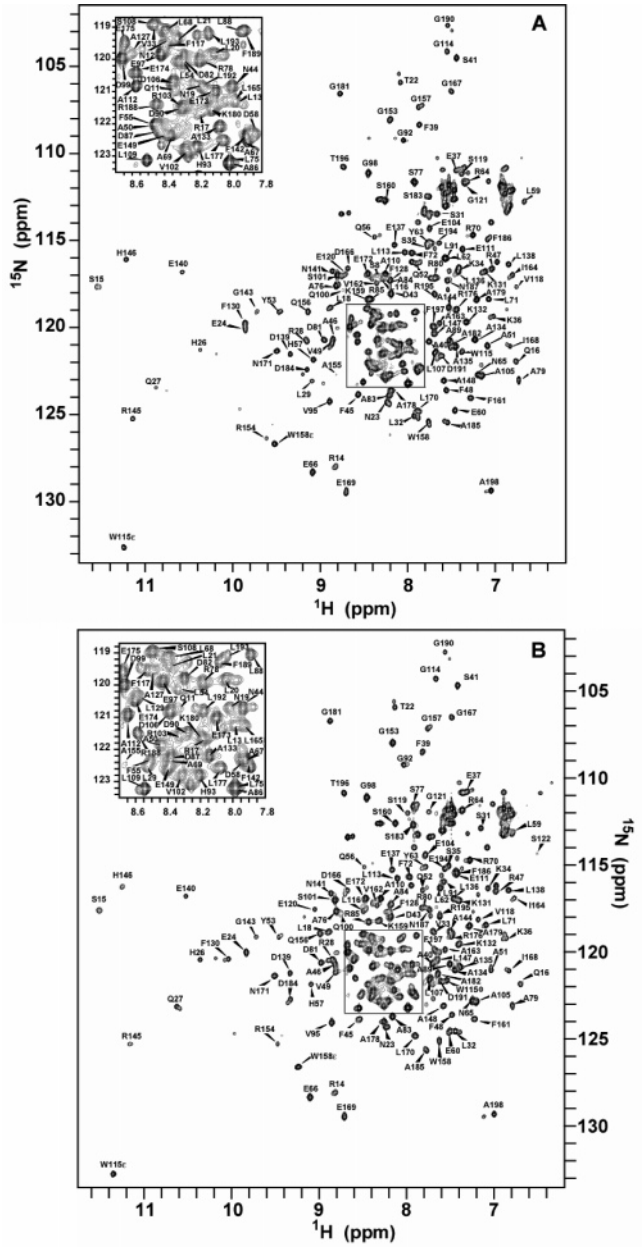

FIGURE 1: Fast ^{1}H{^{15}N} HSQC spectra of 2.8 mM [U-^{15}N]-*pa*-HO (50 mM sodium phosphate, pH 7.0, 5% D_2O) in the presence of 10 equiv of (A) sodium azide and (B) sodium cyanide. The insets show an expanded view of the region delimited by the square, and peak labels indicate the assignment. Spectra were obtained at 305 K using a Bruker Avance800 NMR spectrometer (see Experimental Procedures). Complex points, 256 (t_1) × 2496 (t_2); spectral width, 3 kHz (t_1) × 19.2 kHz (t_2); 4 scans per increment; recycle delay, 1s.

majority of residues in each complex. Labeling with deuterium was unnecessary, and only modest improvement of the line widths of diamagnetic resonances was observed when the ^{1}H-^{15}N heteronuclear correlation spectrum was acquired using a TROSY version of the experiment. Indispensable to our strategy, however, was the use of selective amino acid labeling and NMR experiments acquired with short recycling times, as this strategy was necessary to assign residues strongly affected by the iron paramagnetism (see below). Cross-peaks for 180 out of 190 non-proline backbone amides were observed in the HSQC spectrum of each complex. Amide backbone resonances originating from residues located at the N-terminus region of the protein (Met1, Asp2, Thr3, Glu7, Ser8, Thr9, and Arg10) were either not observed or sufficient data were not available to make a definitive assignment. Assignment of Leu4 and Ala5 was made possible by selectively labeling *pa*-HO with ^{15}N-Leu or ^{15}N-Ala. Resonances from residues Arg42 and Glu151 escaped detection at any of the conditions tested (i.e., temperature, pH, ionic strength, and magnetic field strength), likely due to line broadening caused by conformational exchange.

pa-HO exists in solution as a ~70:30 equilibrium mixture of two isomeric species (*18*), which relate to one another by a 180° rotation of the heme around its $\alpha-\gamma$ meso axis. As a result of heme orientational disorder, several resonances arising from residues located in the heme vicinity exhibit splitting in the HSQC maps. For instance, resonances assigned to His26, Gln27, and Gly190 in Figure 1 show companion peaks of lower intensity and exemplify the effect of heme isomerism on the affected signals. The presence of two heme isomers was initially perceived as a potential source of complication; in the end, however, this phenomenon did not pose major difficulties, and though isomer-specific assignments could be made for the affected residues, only assignments of residues originating from the most abundant isomer in each complex are listed in Table S1 of Supporting Information.

Akin to other bacterial (*17*, *48*) and mammalian (*49*, *50*) heme oxygenases, the structure of *pa*-HO exhibits an α-helical fold (*19*). As expected for an α-helical protein, the ^{1}H-^{15}N HSQC spectra of *pa*-HO−N_3 and *pa*-HO−CN show crowded regions where assignments were difficult to make. Nonetheless, the ambiguities resulting from degeneracy of these resonances were resolved favorably in most cases through analysis of the ^{13}CO shifts obtained from HNCO and (HCA)CO(CA)NH spectra (*51*). Moreover, the latter experiment provided us with the carbonyl ^{13}C shifts of residues preceding a proline (Glu24, Glu37, Glu60, Phe72, His93, and Glu149), that of the C-terminus (Ala198), and Val95, which is flanked by two prolines.

Assignment of Amide Backbone Resonances Near the Heme. Distance measurements performed on the crystal structure of resting state *pa*-HO situate the H_N and N_H atoms of Ser122, Lys123, Leu124, Gly125, and Ala126 at <8 Å from the heme iron. Backbone amide resonances originating from these residues were therefore expected to be strongly influenced by the iron paramagnetism. Indeed, this was manifested in very weak or undetectable cross-peaks in the HSQC spectrum under conditions where all other resonances were clearly observable. To assign these resonances, we resorted to a strategy that entails selective labeling of *pa*-HO with ^{15}N-Gly, ^{15}N-Ala, or ^{15}N-Leu and 2D ^{1}H-^{15}N HSQC or 1D ^{15}N NMR experiments tailored to detect fast-relaxing signals (*52*). Selective labeling of *pa*-HO with ^{15}N-Ala or ^{15}N-Leu using the method reported by Markley et al. (*40*, *52*) resulted in no apparent isotopic scrambling. Application of the same method to the production of *pa*-HO selectively labeled with ^{15}N-Gly, however, resulted in ^{15}N enrichment of every Gly and Ser residue in the protein (Figure S1, Supporting Information). Because only Gly and Ser residues appeared to have been enriched with ^{15}N under these conditions, and since there was no other source of ^{15}N isotope in the culture medium besides ^{15}N-Gly, we hypothesized that

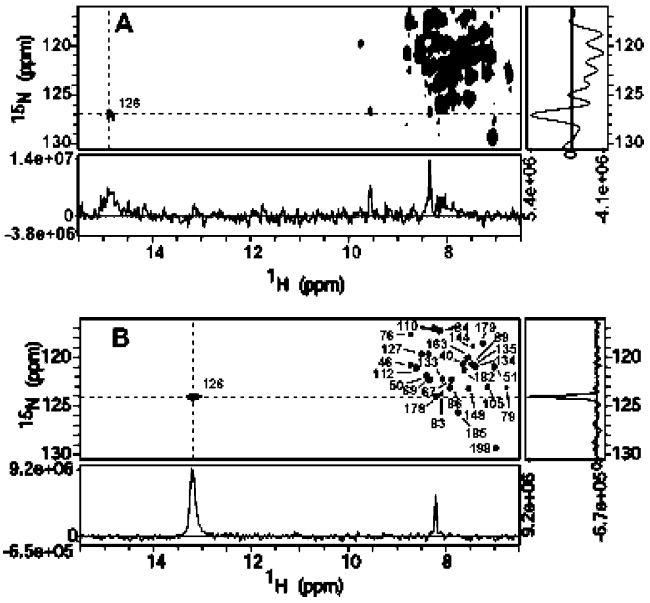

FIGURE 2: ^{1}H{^{15}N} HSQC spectra of the azido (A) and cyano (B) complexes of [^{15}N−Ala]-*pa*-HO. 1D-traces shown at the bottom and right-hand side of each spectrum are taken at cross-peaks originating from Ala126 in each complex. The spectra were obtained at 305 K using a Bruker Avance800 spectrometer. Complex points, 116 (t_1) × 2048 (t_2); spectral width, 2.4 kHz (t_1) × 20.8 kHz (t_2); recycle delay, 200 ms; acquisition time, 65 ms; INEPT transfer delay, 1.6 ms ($^{1}J_{NH}$ = 156 Hz); 128 scans per increment. Data were processed by applying a 90°-shifted, squared sine bell to both dimensions. Linear prediction was applied to extend the time domain size to 256 points in t_1. Data were zero-filled in t_1 and t_2 to yield a data matrix of 512 × 4096. Peak labels indicate the assignment according to the position of the residue in the sequence.

dilution of the ^{15}N label and its incorporation in the protein as Ser may have occurred through a biosynthetic pathway that involves Ser−Gly interconversion in *E. coli* (*53*). Indeed, isotopic scrambling was alleviated by maintaining a high concentration of nonlabeled L-Ser during bacterial growth and protein expression (see Experimental Procedures and Supporting Information). This modification to the expression medium afforded us not only with a way to control the level of ^{15}N-Gly incorporation into *pa*-HO, but also, albeit unintentionally, with a method to produce *pa*-HO labeled exclusively with ^{15}N-Ser and ^{15}N-Gly, which was used in our attempts to establish the identity of Ser122 in *pa*-HO−N_3.

^{1}H-^{15}N HSQC spectra of *pa*-HO−N_3 and *pa*-HO−CN selectively labeled with the aforementioned amino acids are shown in Figures 2, 3, and 5. Samples selectively labeled with ^{15}N-Lys were not prepared, and thus, Lys123 was not assigned in either complex. As most of the assignments were obtained by conventional 3D methods (*54*) (also see Supporting Information), the availability of selectively labeled samples allowed new assignments or confirmed existing ones from correlations of the H_N resonance with the $^{13}C^{\alpha}$, $^{13}C^{\beta}$, or ^{13}CO resonance of the preceding residue or, alternatively, from sequential $NN_{(i,\,i+1)}$ NOEs. Arguments used to carry out the assignments of residues strongly influenced by the iron paramagnetism are presented below.

Assignment of Ala126. The number of cross-peaks found in the spectrum of ^{15}N-Ala *pa*-HO−CN (Figure 2A) or *pa*-HO−N_3 (Figure 2A) is consistent with the number of Ala residues in the protein. Every alanine in the sequence except Ala5 and Ala126 in *pa*-HO−CN and Ala126 in *pa*-HO−N_3 had been previously assigned with the aid of the 3D heteronuclear experiments described in the previous section following the procedure described in Supporting Information. Hence, resonances from previously assigned Ala residues were readily identified in the HSQC spectrum of Figure 2 by comparison with the HSQC spectrum obtained with the uniformly ^{15}N-labeled sample. Alanines at positions 127, 182, and 185 are in relative close proximity to the heme pocket and consequently experience splitting by virtue of heme isomerism. The cross-peak at δ_{1_H} = 13.20 ppm, δ_{15_N} = 124.10 ppm in *pa*-HO−CN (Figure 2B) is broad and exhibits a large downfield ^{1}H shift, which suggest close proximity to the paramagnetic center. These unique features and an $NN_{(i,i+1)}$ NOE contact to the H_N of Ala127 indicate that this cross-peak corresponds to Ala126 in *pa*-HO−CN. With this assignment in hand, the peak at δ_{1_H} = 8.10 ppm and δ_{15_N} = 126.6 ppm was assigned to Ala5 by process of elimination, thus, completing the assignments of Ala residues in *pa*-HO−CN.

Inspection of the *pa*-HO−N_3 HSQC spectrum (Figure 2A) in search of a resonance similar to that of Ala126 in *pa*-HO−CN allowed identification of a cross-peak at δ_{1_H} = 14.80, δ_{15_N} = 126.9 ppm, which is broad relative to other peaks in the spectrum. This feature, and the fact that all other Ala residues in *pa*-HO−N_3 had been previously assigned, identifies it as originating from Ala126. In contrast to the cross-peak originating from Ala126 in *pa*-HO−CN, the corresponding cross-peak in the spectrum of *pa*-HO−N_3 exhibits much lower intensity relative to other resonances in the spectrum; thus, it is visible only when the spectrum is displayed at very low contour levels.

Assignment of Gly125. HSQC spectra obtained from *pa*-HO−N_3 and *pa*-HO−CN selectively labeled with ^{15}N-Gly are shown in Figure 3. Twelve of 13 Gly residues in each complex were assigned using conventional 3D NMR methods (see Supporting Information). Resonances originating from Gly74 and Gly152 in *pa*-HO−CN and *pa*-HO−N_3 exhibit weak intensities with the conditions used to obtain the spectra shown in the figures and consequently are not visible at the contour level shown. The 2D HSQC spectrum obtained with ^{15}N-Gly-labeled *pa*-HO−CN using fast-recycling times shows a cross-peak at δ_{1_H} = 9.10 ppm, δ_{15_N} = 123.0 ppm (Figure 3B), which is significantly broader than the other cross-peaks in the spectrum. This cross-peak can be safely assigned to Gly125 in *pa*-HO−CN because all other Gly residues had been previously assigned with the aid of conventional 3D experiments and because the fast-relaxing signal confirms proximity to the heme iron.

It is noteworthy that an equivalent cross-peak was not observed in the 2D heteronuclear correlation map of ^{15}N-Gly-labeled *pa*-HO−N_3 (Figure 3A), even if the spectrum was acquired using fast-recycling times. This observation suggests that amide NH atoms of Gly125 in *pa*-HO−N_3 are shifted away from the spectral window covered in our HSQC experiments (∼270 to −30 ppm in ^{15}N and 30 to −10 ppm ^{1}H), relax too fast to be detected, or both. It is well-known that the relaxation rates of resonances affected by a paramagnetic center scale with the square of the magnitude of the gyromagnetic ratio. Consequently, the effect on ^{15}N relaxation is reduced ∼100-fold with respect to ^{1}H, which typically makes the effect of paramagnetism on relaxation

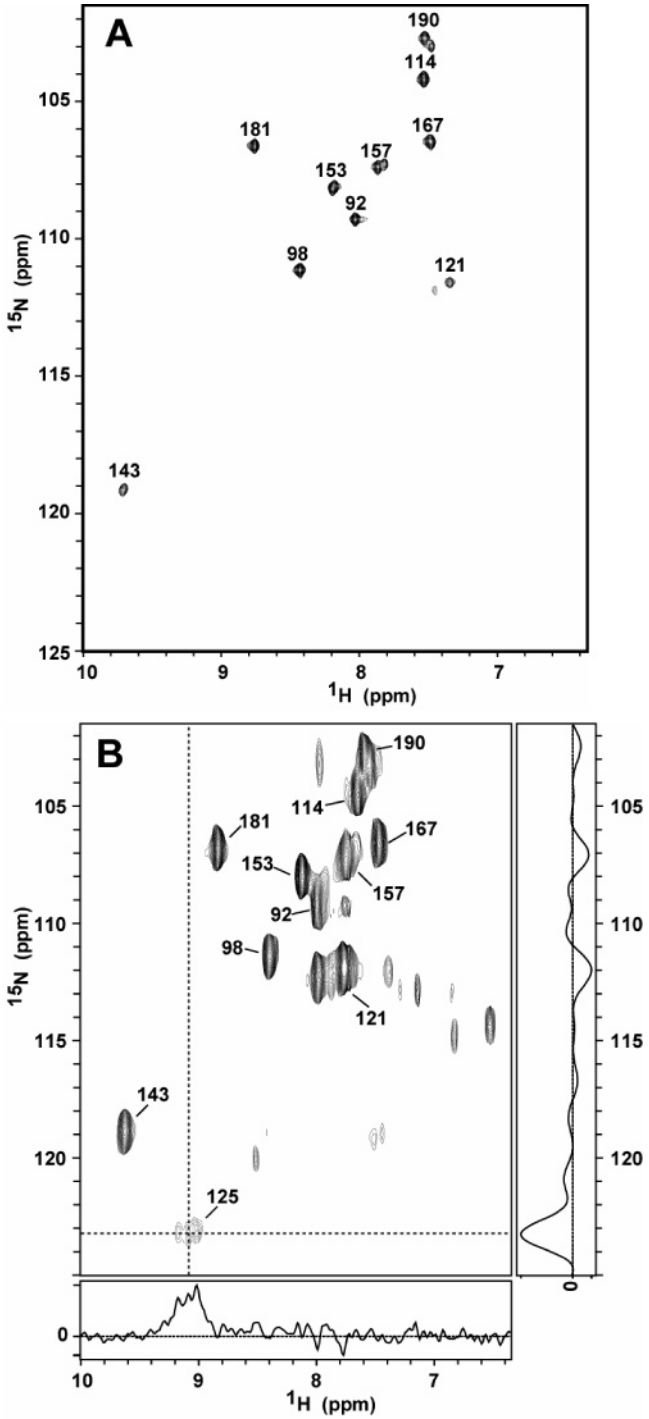

FIGURE 3: ^{1}H{^{15}N} HSQC spectra of the azido (A) and cyano (B) complexes of [^{15}N-Gly]-*pa*-HO. Spectra were recorded on a Bruker Avance800 (A) and Varian Inova600 (B) NMR spectrometers. Acquisition parameters were as follows: (A) complex points, 128 (t_1) × 3328 (t_2); spectral width, 2.1 kHz (t_1) × 19.2 kHz (t_2); relaxation delay, 100 ms; 16 scans. (B) Complex points, 180 (t_1) × 2844 (t_2); spectral width, 12.1 kHz (t_1) × 30 kHz (t_2); acquisition time, 47 ms; recycle delay, 50 ms; 2048 scans. Spectra were processed as indicated in Figure 2.

of ^{15}N nuclei located further than ~7 Å from the heme iron negligible (*55*−*57*). Therefore, loss of signal in a ^{1}H-^{15}N 2D heteronuclear NMR experiment in the presence of a nearby paramagnetic center is most likely a consequence of magnetization loss due to efficient ^{1}H relaxation. We thus attempted assignment of the ^{15}N resonance of Gly125 in *pa*-HO−N_3 by performing 1D ^{15}N NMR experiments with ^{15}N-

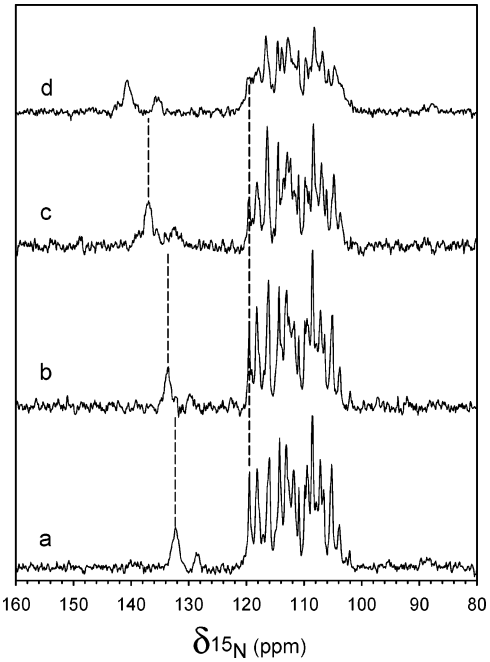

FIGURE 4: One-dimensional ^{15}N NMR spectra of 7 mM [^{15}N-Gly]-*pa*-HO−N_3 obtained at (a) 37, (b) 32, (c) 20, and (d) 8 °C. Spectra were recorded on a Varian Inova600 NMR spectrometer operating at 60.781 MHz. Proton decoupling was not applied, and the following acquisition parameters were used to record each spectrum: spectral width, 21 kHz; acquisition time, 100 ms; relaxation delay, 100 ms; 310 000 scans. Spectra were processed using Varian vnmrJ software. A 10 Hz line broadening and baseline correction were applied.

Gly -labeled *pa*-HO−N_3. Protein concentrations > 7 mM were used to compensate for the inherently low sensitivity of the ^{15}N nucleus. Two peaks stand out in the 1D ^{15}N spectrum of ^{15}N-Gly-labeled *pa*-HO−N_3 (Figure 4a) due to their unusual chemical shifts (128 and 133 ppm at 37 °C) and large line widths. In addition, spectra obtained at different temperatures (Figure 4a−d) show that in the experimentally accessible range (37−8 °C) these peaks exhibit pronounced temperature dependence (linear with inverse temperature), which is clearly distinct from that exhibited by the other ^{15}N Gly resonances. These unique characteristics indicate proximity to the heme iron and therefore identify these ^{15}N peaks as originating from Gly125; the relative intensity of the two broad peaks is in agreement with the presence of a ~70:30 mixture of two heme orientational isomers.

Assignment of Leu124. The spectra in Figure 5 were obtained from samples labeled with ^{15}N-Leu. The spectrum obtained from *pa*-HO−N_3 (Figure 5A) shows a weak cross-peak at ~9.5 ppm ^{1}H shift, which is only visible at low thresholds. The proton line width of this peak is clearly the largest in the spectrum, which suggests that the corresponding proton is in relative proximity to the paramagnetic center. Given that all other Leu residues had been previously assigned with the aid of conventional 3D experiments, the cross-peak at $\delta_{1_H} = 9.50$ ppm, $\delta_{15_N} = 120.6$ ppm is assigned to Leu124 in *pa*-HO−N_3. Assignment of Leu124 in *pa*-HO−CN was made on the basis of a sequential $NN_{(i,\ i+1)}$ NOE to the H_N of Gly125. Interestingly, there is nothing unusual about the chemical shift, intensity, and line width exhibited by the HSQC cross-peak corresponding to Leu124 in *pa*-HO−CN (Figure 5B), which is in marked contrast to the properties exhibited by the cross-peak corresponding to

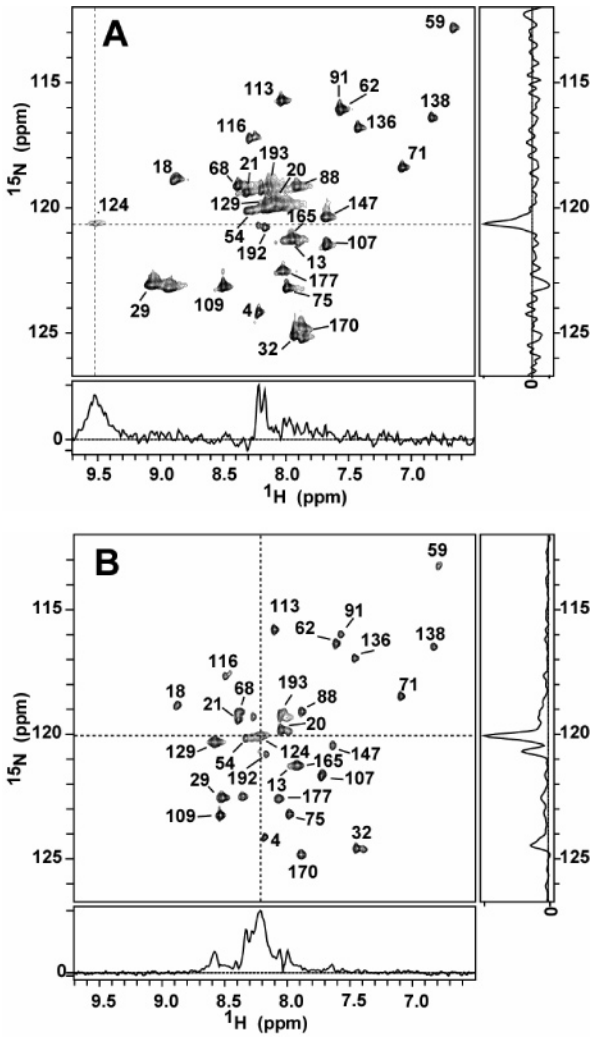

FIGURE 5: ^{1}H{^{15}N} HSQC spectra of the azido (A) and cyano (B) complexes of [^{15}N-Leu]-*pa*-HO. Spectra were recorded on a Bruker Avance800 NMR spectrometer at 305 K. Complex points, 206 (t_1) × 2048 (t_2); spectral width, 2.4 kHz (t_1) × 12.8 kHz (t_2); recycle delay, 80 ms; acquisition time, 65 ms; INEPT transfer delay, 1.6 ms; 128 scans per increment. Processing parameters were as in Figure 2.

Leu124 in *pa*-HO−N_3. These contrasting properties may be indicative of a distinct architecture of the distal heme pocket triggered in response to the nature of the sixth ligand.

Amide H/D Exchange in pa-HO−CN and pa-HO−N_3. Hydrogen−deuterium exchange experiments were carried out in order to probe for the presence of slow conformational dynamics in *pa*-HO−CN and *pa*-HO−N_3 and to establish potential differences between the two complexes. Apparent rates of exchange were determined from the time-dependent disappearance of amide cross-peaks in HSQC spectra obtained after dissolving lyophilized *pa*-HO−CN or *pa*-HO−N_3 in >95% D_2O. Rates of exchange, in turn, were used to calculate protection factors (*46*, *47*) for each of the two *pa*-HO complexes. A per residue plot of protection factors (P), expressed as log P, is shown in Figure 6a,c. To facilitate comparisons between *pa*-HO−CN and *pa*-HO−N_3, data from both complexes are included in the same plot, with red triangles representing values obtained from *pa*-HO−N_3 and blue circles representing values obtained from *pa*-HO−CN. Residues not assigned or corresponding to one of the eight prolines in the sequence do not have an associated symbol in the plot; residues 123−126 do not have an associated symbol in the plot because measurement of the corresponding rates of H/D exchange is rendered not practical by the breadth and, correspondingly, low intensity of their cross-peaks. Symbols at log $P = 1.0$ represent residues whose corresponding cross-peaks are not well-resolved in the HSQC map, and symbols at log $P = 2.0$ represent fast-exchanging residues with experimentally inaccessible values of k_{ex}. Finally, symbols with log $P > 2.0$ correspond to residues exchanging at rates that make measurement of k_{ex} practical.

To facilitate comparison between *pa*-HO−N_3 and *pa*-HO−CN, the difference, calculated as $\Delta\log P = \log P_{N_3} - \log P_{CN}$, where log P_{N_3} and log P_{CN} represent the protection factors for residues in *pa*-HO−N_3, and pa-HO−CN, respectively, has been plotted per residue in Figure 6b,d. In these figures, the horizontal lines at $\Delta\log P \pm 0.47$ represent the average difference obtained from summing the absolute value of $\Delta\log P$ for all residues exhibiting different protection toward exchange. It is also important to note that values of $\Delta\log P = 1.5$ correspond to cases where a residue in *pa*-HO−N_3 exchanges with an experimentally measurable rate constant, but the corresponding residue in pa-HO−CN exchanges too fast to allow measurement of k_{ex}. Thus, although the magnitude of $\Delta\log P$ cannot be evaluated for these residues, they are clearly located in sections of the protein exhibiting the most pronounced differences in their propensity to exchange.

The data in Figure 6b,d reveal that the majority of residues where there is a difference in protection toward exchange exhibit values of $\Delta\log P > 0$, which indicates that on a global scale the backbone amide groups in *pa*-HO−N_3 are distinctively less prone to exchange than their respective counterparts in *pa*-HO−CN. These differences have been mapped on the structure (*19*) of resting state *pa*-HO (Figure 7), where pink highlights residues exhibiting the most protected residues in *pa*-HO−N_3 relative to *pa*-HO−CN ($\Delta\log P = 1.5$), yellow indicates residues with $\Delta\log P >$ average (0.48 in Figure 6b,d), and green indicates residues with $\Delta\log P <$ average. Remarkable about these findings is the fact that the nature of the distal ligand, the diatomic CN^- or the triatomic N_3^-, exerts a large influence on the flexibility of the enzyme, not only in regions of close proximity to the heme but also in portions of the protein that are far removed from the heme iron and distal ligand. Mapping $\Delta\log P$ on the structure of resting state *pa*-HO also reveals that sections of the protein remote from the heme-iron and distal ligand, where there is significantly less flexibility in *pa*-HO−N_3 relative to *pa*-HO−CN, appear to be in "communication" with the distal ligand via a network of structural water molecules (blue in Figure 7). This observation in turn suggests that the network of structural hydrogen-bonded waters plays an important role in propagating structural and dynamic information in heme oxygenase.

DISCUSSION

The Nature of the Distal Ligand Exerts Slight Conformational Changes and Divergent Dynamic Behavior. Previous NMR spectroscopic studies of the heme active site in HO led us to suggest that coordination of a distal ligand capable of accepting a proton to form a hydrogen bond at the coordinating atom, that is, OH^- or N_3^-, induces unusual

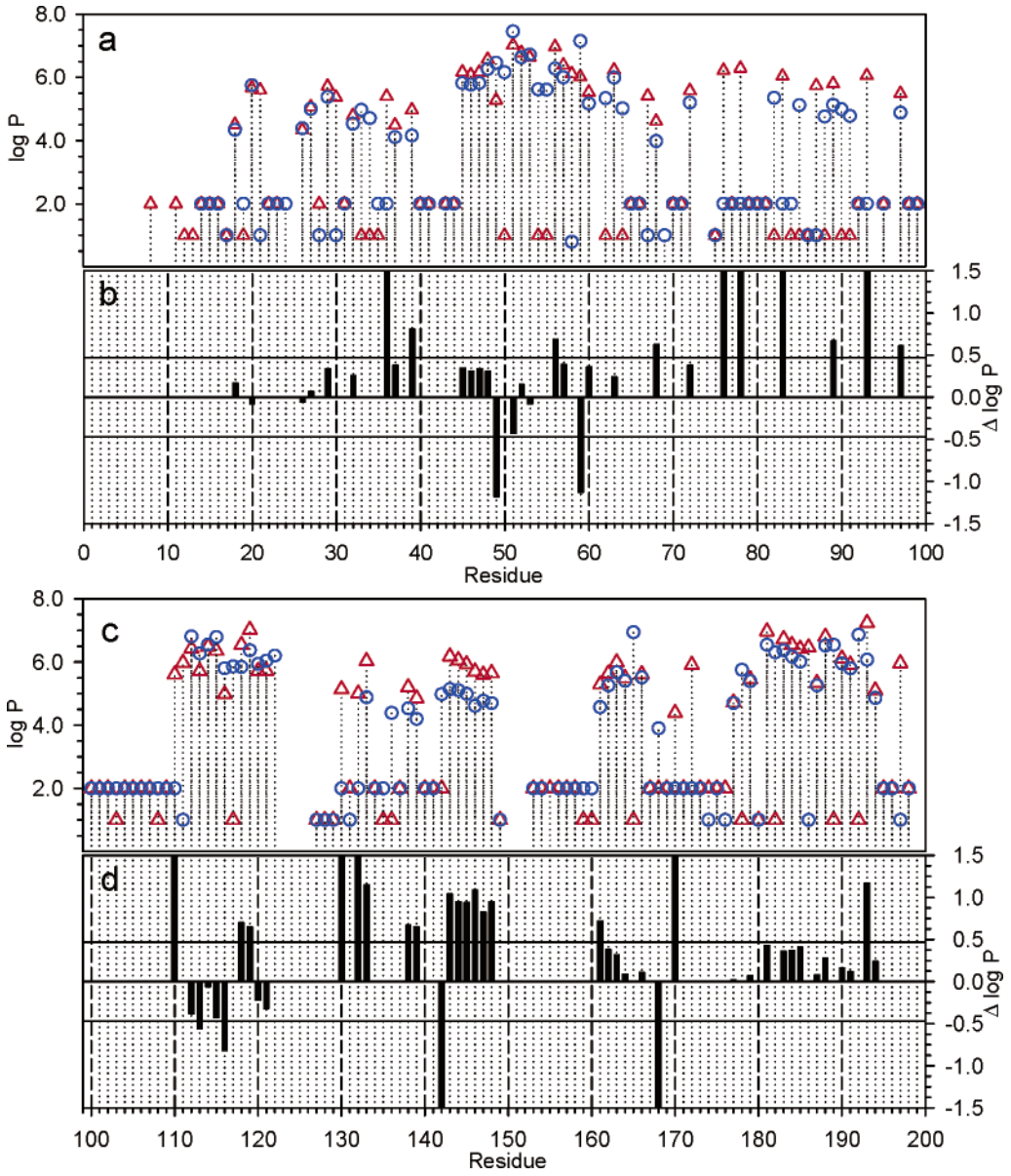

FIGURE 6: (a and c) Per residue protection factors obtained from amide H/D exchange experiments with *pa*-HO−N_3 (red triangles) and *pa*-HO−CN (blue circles). A value of log $P = 2$ was arbitrarily given to residues exhibiting exchange rates too fast to be measured, and a value of log $P = 1$ was given to residues not included in the analysis due to either peak overlap or lack of assignments. (b and d) Per residue differences in protection factors ($\Delta\log P = \log P_{azide} - \log P_{cyanide}$) between the *pa*-HO−$N_3$ and *pa*-HO−CN. The average difference of all residues is indicated by the horizontal line. Bars reaching the maximum vertical scale ($\Delta\log P = 1.5$) correspond to residues exhibiting exchange rates measurable in *pa*-HO−N_3 but too fast to measure in the *pa*-HO−CN (not included in the computation of the average difference).

heme electronic structures and nonplanar distortions of the heme macrocycle (*30*, *31*). Axial coordination of a hydroperoxo ligand, which is capable of accepting a proton to form a hydrogen bond at the coordinated oxygen atom, is therefore expected to induce similar electronic structures with unpaired spin density at the meso carbons in the Fe^{III}−OOH intermediate of HO. Unpaired spin density at the meso carbons, in turn, is expected to activate these positions and help in directing the homolytic cleavage of the O−O bond so that ·OH is trapped by a sterically unprotected meso carbon to yield *meso*-hydroxyheme, the first committed intermediate in the path to biliverdin (Scheme 2). In contrast, coordination of CN^-, which is not capable of accepting a proton to form a hydrogen bond at the coordinating carbon, results in HO complexes exhibiting planar heme and an electronic structure ($S = 1/2$, d_π) that places negligible unpaired spin density at the meso carbons (*18*, *58*). Given that *pa*-HO−OH and pa-HO−N_3 are reasonable models of the highly reactive *pa*-HO−OOH intermediate, we decided to take advantage of the fact that *pa*-HO−N_3 can be prepared at neutral pH to extend our NMR spectroscopic investigations from the heme active center to the polypeptide. Hence, an important aim of this study is to determine whether the pronounced differences in heme conformation and electronic structure observed with *pa*-HO−CN and *pa*-HO−N_3 are also manifested in different structural and dynamical properties of the polypeptide associated with each of these HO complexes.

Chemical shift perturbation analysis of backbone resonances has been widely used as a probe to identify residues experiencing altered chemical properties as a consequence of protein−protein interactions (*59*). In this study, the magnitude of amide chemical shift perturbation occurring

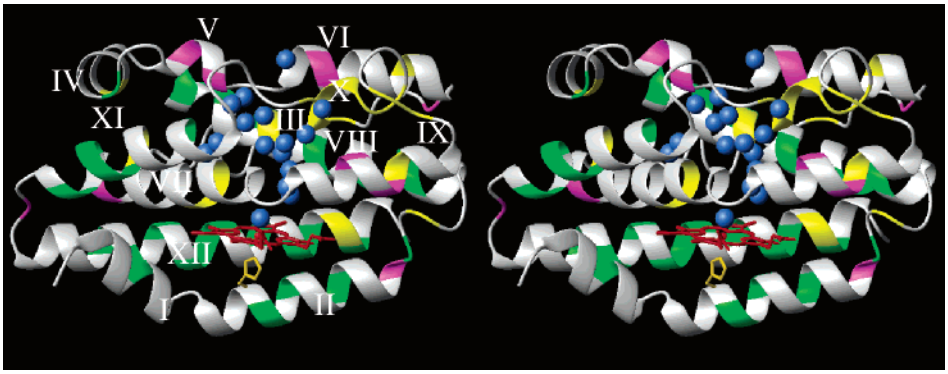

FIGURE 7: Stereoview of resting state of *pa*-HO highlighting regions in which *pa*-HO−N_3 exhibits enhanced protection to exchange relative to pa-HO−CN (positive $\Delta\log P$ in Figure 6). Sections exhibiting $0 < \Delta\log P < 0.47$ are green, $0.47 < \Delta\log P < 1.5$ are yellow, and $\Delta\log P = 1.5$ are pink. $\Delta\log P = 1.5$ identifies residues exhibiting the most pronounced differences in exchange behavior because it highlights residues in *pa*-HO−N_3 exchanging at measurable rates, but the corresponding residues in *pa*-HO−CN exchange at rates too fast to measure. $\Delta\log P \pm 0.48$ represents the average difference obtained from all residues exhibiting different protection factors in *pa*-HO−N_3 and *pa*-HO−CN. The heme is colored red, and the proximal ligand (His26) is shown in orange. Water molecules are colored blue and are shown as they appear in the X-ray structure (PDB: 1SK7).

upon replacing the N_3^- ligand for CN^- was used as an indicator of regions in the protein experiencing altered chemical environments of their amide nuclei as a result of ligand replacement. The data reveal clear differences in amide and carbonyl chemical shifts between the two complexes (Figure 8). The magnitude of these changes, as determined by the weighted average chemical shift difference of amide ^1H and ^{15}N nuclei, has been plotted per residue in Figure 8a and mapped onto the structure of resting state *pa*-HO in Figure 8c. Regions of secondary structure highlighted in blue harbor residues exhibiting average shift perturbations larger than the arithmetic mean of all perturbations (0.06 ppm) but ≤0.2 ppm. Regions of secondary structure highlighted in orange harbor residues exhibiting the largest shift perturbations (>0.2 ppm). Inspection of carbonyl chemical shift perturbations brought about by ligand replacement (Figure 8b) reveals that amide and carbonyl chemical shift perturbations occur in nearly the same elements of secondary structure, suggesting that *pa*-HO−CN and *pa*-HO−N_3 indeed exhibit distinct conformational properties. It is important to point out, however, that elements of secondary structure, as evaluated from the chemical shift index analysis (*60*) of the two complexes (Figure S4, Supporting Information), indicate conservation of secondary structure. Consequently, the conformational differences reported by the chemical shifts are likely small. Understanding these small conformational changes awaits efforts currently in progress aimed at solving the structures of *pa*-HO−N_3 and *pa*-HO−CN.

Residues exhibiting the largest amide chemical shift perturbations (orange in Figure 8) are mostly clustered in the proximal helix (residues 28 and 31−34 in helix II), beyond the coordinating histidine (His26), and in the last turn of the distal helix, before the helix kink (residues 118−121 in helix VII). Perturbation of chemical shifts corresponding to residues 118−121 is perhaps not surprising because this is the region of the polypeptide that is closer to the distal ligand. In the structure of rat-HO−N_3, this region is known to provide the steric push that forces the azide group toward the meso carbon susceptible to hydroxylation, *δ*-meso in *pa*-HO (*36*). The chemical shift changes in the proximal helix, on the other hand, are surprising because they extend to residues relatively far from the coordinating histidine and therefore cannot be explained by heme paramagnetism. It is also interesting that chemical shift perturbations above the arithmetic average (blue) are observed for residues located in all elements of secondary structure surrounding the heme. This interesting observation appears to be a manifestation of the ability of HO to adapt to the demands of the catalytic cycle, which include changes in distal ligand (H_2O, O_2, HOO^-) and changes in substrate structure (heme, hydroxyheme, verdoheme, and biliverdin) with minimum local structural perturbations.

Observations made with H/D exchange experiments complement the chemical shift perturbation data in that they suggest that the nature of the distal ligand brings about relatively large changes in dynamic properties with relatively minor changes in structure. Interpretation of exchange rates in terms of protection factors permits quantitative comparison of differences in the susceptibility of amide bonds to undergo H/D exchange reactions under specific conditions. These differences in exchange susceptibility, in turn, are likely related to divergent dynamic behavior. In this context, a comparative analysis of the protection factors obtained for *pa*-HO−CN and *pa*-HO−N_3 (Figures 6 and 7) reveals that *pa*-HO−N_3 is significantly less prone to hydrogen−deuterium exchange reactions than *pa*-HO−CN at the time scales probed by H/D exchange experiments. Among residues that are most protected in *pa*-HO−N_3 relative to *pa*-HO−CN (pink and yellow in Figure 7), those located in helices V, VI, and X and the loop preceding helix X stand out because they are in the periphery of the molecule remote from the heme iron and the distal ligand. Moreover, inclusion of the crystallographic structural waters (blue) in the model of Figure 7 strongly suggests the possibility that long-range communication between the distal ligand and helices V, VI, and X occurs via these networked structural waters. This hydrogen bond network is thought to function as an integral part of a proton delivery machinery used by HO to protonate the nascent $Fe^{III}-OO^-$ moiety in the process of oxygen activation that leads to meso-carbon hydroxylation (*25*, *61*). Our findings derived from the H/D exchange experiments indicate that proton delivery is not the only function of the network of hydrogen-bonded water molecules. Instead, the data suggest that an additional function is to provide adaptable interactions between otherwise remote structural elements, thus, permitting rapid propagation of conforma-

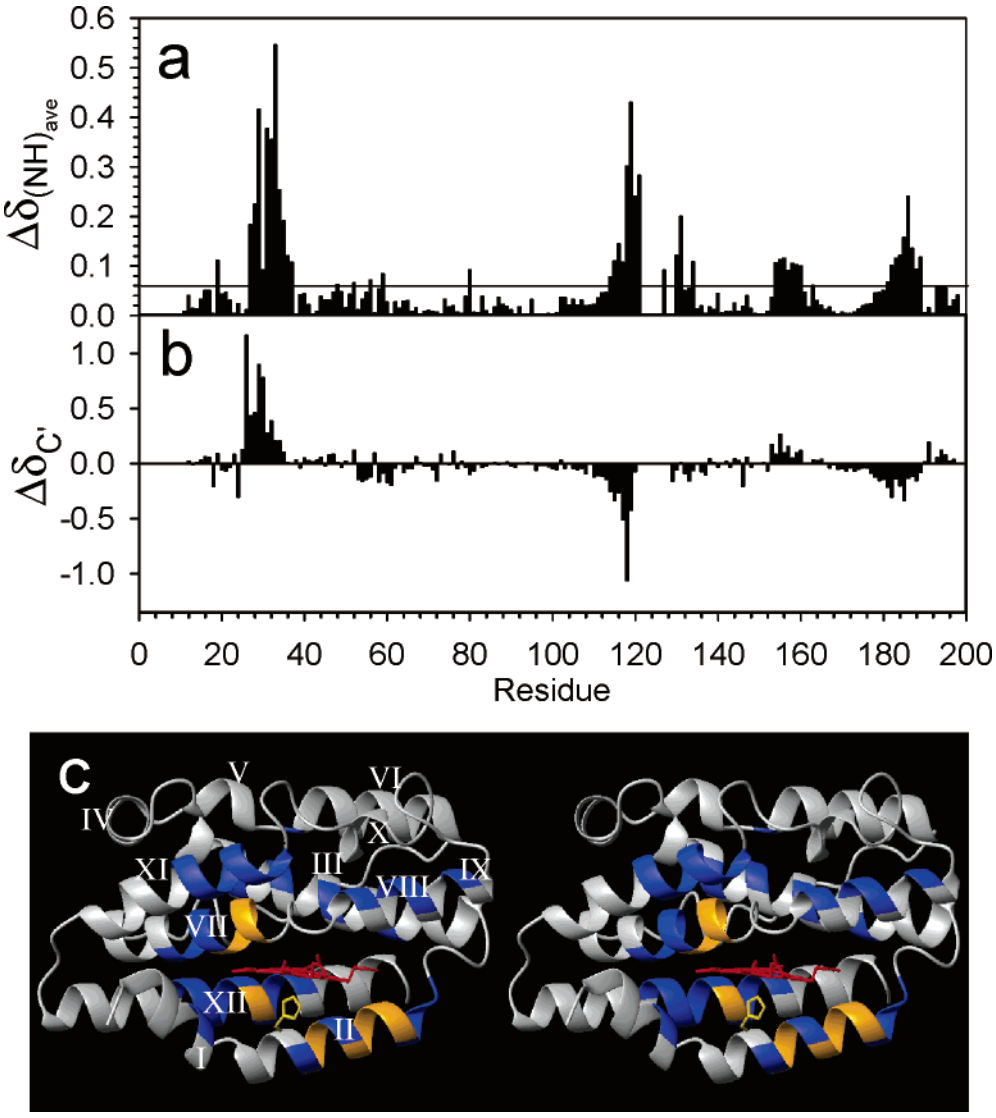

FIGURE 8: Per residue chemical shift difference expressed as $\Delta\delta$, obtained by subtracting the chemical shift of a residue in *pa*-HO−CN from the corresponding chemical shift in *pa*-HO−N_3. (a) Difference in amide chemical shifts represent the weighted average of ^1H and ^{15}N shifts and was calculated with the expression $\Delta\delta_{ave} = \{[(\Delta\delta_{1_H})^2 + (\Delta\delta_{15_N}/5)^2]/2\}^{1/2}$. The average difference of all residues (0.06) is indicated by a horizontal line. (b) Per residue difference in carbonyl (C′) chemical shifts. (c) Weighted average amide chemical shift differences mapped onto the structure of resting state *pa*-HO (ID: 1SK7). Elements of secondary structure identified as α-helices are labeled with roman numerals. Residues found to exhibit the largest differences ($\Delta\delta_{ave} > 0.2$) are in orange, and those exhibiting differences in the range $0.06 < \Delta\delta_{ave} < 0.2$ are shown in blue. The heme is shown in red and the side chain of His26 in yellow.

tional changes in the active site with minimum perturbation of secondary structure. In other words, the versatile interactions provided by the networked structural waters impart the enzyme with the plasticity necessary to adapt to the demanding changes imposed by the catalytic cycle, which encompass changes in distal ligand and the gradual dismantling of a large substrate (heme) into *meso*-hydroxy heme, verdoheme, and biliverdin. A more detailed dynamic study of *pa*-HO−N_3 and *pa*-HO−CN is necessary to test this hypothesis. These studies are currently underway in our laboratory.

The Issue of a Hydrogen Bond to the Coordinated Azide and Its Effect on Heme Electronic Structure. Zeng et al. have recently shown that the heme in *pa*-HO−N_3 exhibits ^{13}C NMR spectra consistent with an equilibrium mixture of spin states, $S = 1/2$, d_π and $S = 3/2$, $(d_{xz}, d_{yz})^3(d_{xy})^1(d_z^2)^1$, which differs from the pure $S = 1/2$, d_π electron configuration typical of cyanide-inhibited hemoproteins, including *pa*-HO−CN (*31*). The presence of unpaired electron density in the d_z^2 orbital should be manifested in spin delocalization to the axial ligands, N_3^- and His26. It is therefore interesting that the ^{13}C chemical shift corresponding to C_β in His26 of *pa*-HO−N_3 is 40.5 ppm, a value significantly larger than those exhibited by ferrihemes with a pure $S = 1/2$, d_π electron configuration. Examples of the latter complexes are *pa*-HO−CN (24.64 ppm, Table 1), rat outer membrane cytochrome b_5 (21.4 ppm for His39 and 17.8 ppm for His63) (*45*), and hexacoordinated hemoglobin from *Synechocystis* sp. PCC 6803 (24.3 ppm for His46 and 23.8 ppm for His70) (*62*). Hence, at 40.5 ppm, the C_β of His26 is significantly shifted from the average C_β chemical shift (22.4 ± 2.9 ppm) observed for axial histidine ligands coordinated to a ferric heme with an $S = 1/2$, d_π electron configuration and is consistent with through-bond delocalization of electron spin density present in the d_z^2 orbital of the $S = 3/2$, $(d_{xz}, d_{yz})^3(d_{xy})^1(d_z^2)^1$ *pa*-HO−N_3 complex.

As indicated above, heme-centered NMR work conducted with *pa*-HO−OH and *pa*-HO−N_3 led to the conclusion that the unusual heme electronic structures of these *pa*-HO

Table 1: Line Widths and Chemical Shifts of Resonances from Residues in Close Proximity to the Heme Iron in *pa*-HO−CN and *pa*-HO-N_3[a]

	L124		G125		A126	
	CN^-	N_3^-	CN^-	N_3^-	CN^-	N_3^-
line width (Hz)	105.1 (31.7)	91 (34.0)	149.2 (36.6)	ND (29.1)	67.7 (29.0)	92.6 (33.3)
δ^1H (ppm)	8.2 (7.9)	9.5 (7.9)	9.1 (8.3)	ND (8.3)	13.2 (7.9)	14.8 (7.9)
δ^{15}N (ppm)	120.1 (119.7)	120.6 (119.7)	123.0 (109.7)	132.7 (109.7)	124.1 (121.6)	126.9 (121.7)

[a] Average line widths and chemical shift values of residues of the same type are given in parentheses. ^{1}H line widths were estimated from cross-peaks in HSQC spectra. The amide hydrogen of Gly125 in *pa*-HO−N_3 was not detected (ND).

complexes are a consequence of decreased axial ligand (OH^- or N_3^-) field strength. It was proposed that the lower than typical field strength of OH^- and N_3^- coordinated to *pa*-HO likely stems from accepting a proton to form a hydrogen bond at the coordinating atom; the donor would be either a H_2O molecule or a backbone N−H (*28*, *30*, *31*). The crystal structure of rat-HO-1 in complex with azide shows that conserved Gly143 donates a hydrogen bond to the coordinating atom of the distal N_3^- ligand (*36*). The equivalent residue in *pa*-HO is Gly125; thus, we were interested in determining whether Gly125 N−H forms a hydrogen bond with the coordinated N atom in *pa*-HO−N_3. Below, we discuss evidence that strongly suggests the presence of such hydrogen-bonding interaction.

Chemical shift and line width data for residues located above the heme near the iron in the structure of resting state *pa*-HO are shown in Table 1; the corresponding average values obtained from all other residues of the same type are given in parentheses. The proximity of Leu124 and Ala126 to the heme iron is evident in the width of the amide ^{1}H resonances, which are at least 3-fold broader than the average obtained from other residues of the same type in each complex. Although the ^{1}H resonance of Gly125 could not be detected, the corresponding ^{15}N resonance is broad, suggesting that the ^{1}H resonance is broadened beyond detection. The corresponding ^{15}N resonance, observed in 1D experiments (see Figure 4), is 3-fold broader than other ^{15}N resonances in *pa*-HO−N_3, is significantly downfield-shifted relative to other Gly ^{15}N−H resonances, and exhibits pronounced temperature dependence. These unusual properties of the ^{15}N resonance suggest through-bond (Fermi contact) spin delocalization from the heme iron into the Gly125 ^{15}N atom. A Fermi contact interaction would only be possible if the Gly125 N−H forms a hydrogen bond with the iron-bound nitrogen of azide. Similar contact interactions have been reported for *Clostridium pasteurianum* rubredoxin and other proteins (*63*) on the basis of large and atypical ^{15}N chemical shifts originating from residues not directly bound to the metal. These ^{15}N resonances also exhibit a larger than usual, upfield deuterium isotope effects. By means of density functional theory (DFT) calculations, Markley and co-workers were able to replicate the magnitude and direction of the upfield deuterium isotope effect and concluded that residues displaying such a behavior participate in H-bonds formed between amide ^{15}N-^{1}H and the metal-bound sulfur atom of Cys residues (*63*, *64*).

With the aim of observing an unusual upfield deuterium isotope effect on the ^{15}N resonance of Gly125, we obtained 1D ^{15}N NMR spectra of [^{15}N-Gly]-*pa*-HO−N_3 dissolved in D_2O (Figure 9). These spectra show noticeable changes in the overall distribution and features of peaks relative to the spectrum in H_2O. For example, peaks resonating in the 100−120 ppm window exhibit decreased intensity in D_2O relative to spectra in H_2O, but no apparent chemical shift changes. In contrast, the most downfield-shifted peaks originating from Gly125 exhibit a 2 ppm upfield deuterium isotope shift at 37 °C, which is accompanied by a clear decrease in line width relative to the spectrum in water. The deuterium isotope shift is of similar magnitude at 20 °C and was found to be pH-independent. To place these observations in context, it is important to note that deuterium isotope effects on ^{15}N amide shifts in diamagnetic proteins are typically manifested in increased shielding contributions to the isotropic shift, thus, resulting in upfield shifted peaks (*65*). The magnitudes of these upfield shifts, however, are of the order of at most 0.7 ppm for residues in α-helical proteins (*65*). Hence, at 2 ppm, the upfield deuterium isotope effect exhibited by the Gly125 ^{15}N resonance strongly suggests hydrogen bond-mediated delocalization of unpaired spin density from the heme iron to the ^{15}N atom of Gly125. The magnitude of this deuterium isotope effect is relatively small compared with that observed in *C. pasteurianum* rubredoxin (>8 ppm). The differences in magnitude, however, may be explained by potential differences in the H-bond strength and by different spin delocalization mechanisms exhibited by heme and the iron sulfur cluster of rubredoxin. In addition, the documented isotope effects pertain to Val, Tyr, and Leu residues (*65*), all of which exhibit lower ^{15}N shieldings and thus resonate at higher ^{15}N frequencies (downfield) than Gly residues. Thus, the increased shielding of ^{15}N in Gly would counter-

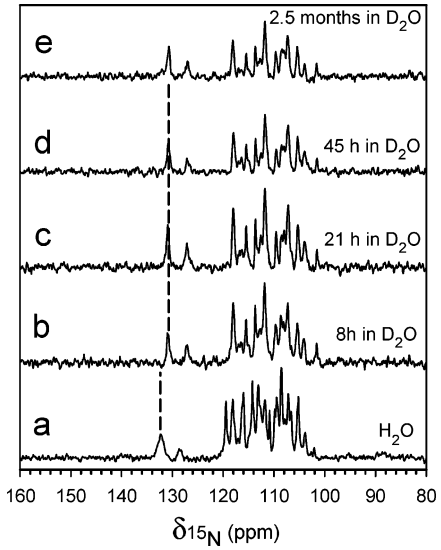

FIGURE 9: One-dimensional ^{15}N NMR spectra of 7 mM [^{15}N-Gly]-*pa*-HO−N_3 obtained upon exchanging the aqueous solvent for D_2O. Acquisition and processing parameters are as in Figure 4, except that 160 000 scans were averaged. The time indicated on the right-hand side of each spectrum represents the time elapsed from solvent exchange to the end of acquisition of the corresponding spectrum.

balance the isotope effect shift, resulting in smaller upfield isotope effect shifts for Gly residues (*65*). The absence of a structure for *pa*-HO−N_3 currently prevents calculation of the deuterium isotope effect experienced by the Gly125 ^{15}N nucleus participating in the proposed H-bond. Nevertheless, observation of an upfield deuterium isotope effect significantly larger than that expected for a diamagnetic protein complements the large downfield shift of the Gly125 ^{15}N resonance and its pronounced temperature dependence as indicators of Fermi contact interactions. This argues strongly in favor of the presence of a hydrogen bond between Gly125 N−H and the coordinating azide nitrogen. The effect of this hydrogen bond is to lower the ligand field strength of the axial azide ligand, which promotes the unusual heme electronic structure of pa-HO−N_3 (*31*). In closing this section, it is important to mention that the present evidence may also be consistent with a hydrogen bond between the Gly125 N−H and a water molecule, which in turn is hydrogen-bonded to the coordinated azide nitrogen (Gly125 N−H−OH_2−N_3-Fe^{III}). In this scenario, unpaired spin density may be delocalized from the heme iron to the Gly125 N−H via two hydrogen bonds.

Concluding Remarks. Heme hydroxylation as catalyzed by HO occurs via an obligatory Fe^{III}−OOH intermediate (Scheme 1), which is thought to add a hydroxyl group to a meso carbon (*25*, *66*). This reaction is distinct from that typically exhibited by cytochromes P450 and peroxidases which employ ferryl (Fe^{IV}═O) to carry out substrate oxidation (*26*). Paradoxically, computational work suggest that the Fe^{III}−OOH complex does not have enough oxidizing power to warrant heme hydroxylation via concerted electrophilic attack to the heme meso position (*67*), as originally proposed (*24*, *68*). Additional computational studies led to the conclusion that heme hydroxylation must take place via either homolytic cleavage of the O−O bond to produce ·OH radical which is efficiently trapped by a meso carbon (*35*) or, alternatively, via the formation of a water-bridged oxo intermediate (*69*). Experimental work carried out with model heme complexes and with *pa*-HO−OH and *pa*-HO−N_3 as models of the highly reactive Fe^{III}−OOH intermediate revealed nonplanar hemes with unusual electronic structures that place unpaired spin density at the meso carbons (*30*, *31*). Hence, the seemingly paradoxical computational result indicating that the Fe^{III}−OOH does not have enough oxidizing power would be explained by unpaired spin density, which is expected to activate the reactivity of meso carbons, thus, lowering the energy barrier for hydroxylation. Moreover, the unpaired spin density at meso carbons would assist in a radical mechanism (*29*−*31*), a hypothesis that is complementary to ideas stemming from computational work (*35*), which suggest trapping of a ·OH radical by a sterically nonprotected meso carbon. In this study we have aimed at interrogating the polypeptide with the goal of probing whether the nature of the distal ligand also affects the polypeptide. The results suggest that the nature of the distal ligand induces small conformational changes in all elements of secondary structure surrounding the heme. Surprisingly, the nature of the distal ligand exerts significant changes in amide protection factors, which we interpret to indicate that the polypeptide in *pa*-HO−N_3 is less flexible than the polypeptide in *pa*-HO−CN. Consequently, the differences in heme electronic structure between *pa*-HO−CN and *pa*-HO−N_3 appear to be sensed by the polypeptide. Propagation of this information to remote regions of the polypeptide is likely carried out by a network of hydrogen-bonded water molecules. Hence, a proposed new function for these structural waters is to impart enzyme adaptability to the demanding changes of the catalytic cycle with minor changes in secondary structure. These new ideas invoking dynamics and reactivity must be tested rigorously. Future work in this direction will be facilitated by the availability of nearly complete sequential assignments for this 198-amino acid paramagnetic enzyme. Finally, the relatively large downfield shift, the large temperature dependence, and the upfield deuterium isotope effect characteristic of the Gly125 ^{15}N resonance in *pa*-HO−N_3 support the notion of a hydrogen bond between the coordinated azide nitrogen and the amide hydrogen of Gly125. The presence of this hydrogen bond would lower the ligand field strength of the N_3^- ligand, which has the effect of inducing the unusual heme electronic structure and nonplanar heme distortions observed in *pa*-HO−N_3 (*31*).

SUPPORTING INFORMATION AVAILABLE

NMR data including an HSQC spectrum of [^{15}N-Gly, ^{15}N−Ser]-*pa*-HO−N_3 and representative strip plots of HNCA, HN(CO)CA, HNCACB, CBCA(CO)NH, HNCO, and (HCA)-CO(CA)NH spectra; text describing the general strategy used to carry out sequential resonance assignments of regions not strongly affected by the heme iron paramagnetism; CSI plots of *pa*-HO−N_3 and *pa*-HO−CN; and a table listing the assignments. This material is available free of charge via the Internet at http://pubs.acs.org.

REFERENCES

1. Tenhunen, R., Marver, H. S., and Schmid, R. (1969) Microsomal heme oxygenase. characterization of the enzyme, *J. Biol. Chem. 244*, 6388−6394.
2. Uzel, C., and Conrad, M. E. (1998) Absorption of heme iron, *Semin. Hematol. 35*, 27−34.
3. Maines, M. D. (1997) The heme oxygenase system: a regulator of second messenger gases, *Annu. Rev. Pharmacol. Toxicol. 37*, 517−554.
4. Stocker, R., Yamamoto, Y., McDonagh, A. F., Glazer, A. N., and Ames, B. N. (1987) Bilirubin is an antioxidant of possible physiological importance, *Science 235*, 1043−1046.
5. Marilena, G. (1997) New physiological importance of two classic residual products: carbon monoxide and billirubin, *Biochem. Mol. Med. 61*, 136−142.
6. Verma, A., Hirsch, D. J., Glatt, C. E., Ronnett, G. V., and Snyder, S. H. (1993) Carbon monoxide: a putative neural messenger, *Science 259*, 381−384.
7. Wilks, A., and Schmitt, M. P. (1998) Expression and characterization of a heme oxygenase (Hmu O) from *Corynebacterium diphtheriae*, *J. Biol. Chem. 273*, 837−841.
8. Zhu, W., Hunt, D. J., Richardson, A. R., and Stojiljkovic, I. (2000) Use of heme compounds as iron sources by pathogenic *Neisseriae* requires the product of the *hemO* gene, *J. Bacteriol. 182*, 439−447.
9. Schmitt, M. P. (1997) Utilization of host iron sources by *Corynebacterium diphteriae*: identification of a gene whose product is homologous to eukaryotic heme oxygenases and is required for acquisition of iron from heme and hemoglobin, *J. Bacteriol. 179*, 838−845.
10. Ratliff, M., Zhu, W., Deshmukh, R., Wilks, A., and Stojiljkovic, I. (2001) Homologues of Neisserial heme oxygenase in gram-negative bacteria: degradation of heme by the product of the *pigA* gene of *Pseudomonas aeruginosa*, *J. Bacteriol. 183*, 6394−6403.
11. Skaar, E. P., Gaspar, A. H., and Schneewind, O. (2004) IsdG and IsdI, heme-degrading enzymes in the cytoplasm of *Staphylococcus aureus*, *J. Biol. Chem. 279*, 436−443.

12. Pendrak, M. L., Chao, M. P., Yan, S. S., and Roberts, D. D. (2004) Heme oxygenase in *Candida albicans* is regulated by hemoglobin and is necessary for metabolism of exogenous heme and hemoglobin to α-biliverdin, *J. Biol. Chem. 279*, 3426−3433.
13. Suits, M. D., Pal, G. P., Nakatsu, K., Matte, A., Cygler, M., and Jia, Z. (2005) Identification of an *Escherichia coli* 0157:H7 heme oxygenase with tandem functional repeats, *Proc. Natl. Acad. Sci. U.S.A. 102*, 16955−16960.
14. Chu, G. C., Tomita, T., Sönnichsen, F. D., Yoshida, T., and Ikeda-Saito, M. (1999) The heme complex of Hmu O, a bacterial heme degradation enzyme from *Corynebacterium diphtheriae*, *J. Biol. Chem. 274*, 24490−24496.
15. Hirotsu, S., Chu, G. C., Unno, M., Lee, D.-S., Yoshida, T., Park, S.-Y., Shiro, Y., and Ikeda-Saito, M. (2004) The crystal structures of the ferric and ferrous forms of the heme complex of HmuO, a heme oxyenase of *Corynebacterium diphtheriae*, *J. Biol. Chem. 279*, 11937−11947.
16. Zhu, W., Wilks, A., and Stojiljkovic, I. (2000) Degradation of heme in gram-negative bacteria: the product of the *hemO* gene of *Neisseriae* is a heme oxygenase, *J. Bacteriol. 182*, 6783−6790.
17. Schuller, D. J., Zhu, W., Stojiljkovic, I., Wilks, A., and Poulos, T. L. (2001) Crystal structure of heme oxygenase from the gram-negative pathogen *Neisseria meningitidis* and a comparison with mammalian heme oxygenase, *Biochemistry 40*, 11552−11558.
18. Caignan, G. A., Deshmukh, R., Wilks, A., Zeng, Y., Huang, H., Moënne-Loccoz, P., Bunce, R. A., Eastman, M. A., and Rivera, M. (2002) Oxidation of heme to *β*- and *δ*-biliverdin by *Pseudomonas aeruginosa* heme oxygenase as a consequence of an unusual seating of the heme, *J. Am. Chem. Soc. 124*, 14879−14892.
19. Friedman, J., Lad, L., Li, H., Wilks, A., and Poulos, T. L. (2004) Structural basis for novel *δ*-regioselective heme oxygenation in the opportunistic pathogen *Pseudomonas aeruginosa*, *Biochemistry 43*, 5239−5245.
20. Costerton, J. W., Stewart, P. S., and Greenberg, E. P. (1999) Bacterial biofilms: a common cause of persistent infection, *Science 284*, 1318−1322.
21. Ochsner, U. A., Johnson, Z., and Vasil, A. I. (2000) Genetics and regulation of two distinct haem-uptake systems, *phu* and *has*, in *Pseudomonas aeruginosa*, *Microbiology 146*, 185−198.
22. Vasil, M. L., and Ochsner, U. A. (1999) The response of *Pseudomonas aeruginosa* to iron: genetics, biochemistry and virulence, *Mol. Microbiol. 34*, 399−413.
23. Ortiz de Montellano, P. R., and Wilks, A. (2000) Heme oxygenase structure and mechanism, *Adv. Inorg. Chem. 51*, 359−407.
24. Wilks, A., and Ortiz de Montellano, P. R. (1993) Rat liver heme oxygenase, *J. Biol. Chem. 268*, 22357−22362.
25. Davydov, R., Kofman, V., Fujii, H., Yoshida, T., Ikeda-Saito, M., and Hoffman, B. M. (2002) Catalytic mechanism of heme oxygenase through EPR and ENDOR of cryoreduced oxy-heme oxygenase and its Asp 140 mutants, *J. Am. Chem. Soc. 124*, 1798−1808.
26. Sono, M., Roach, M. P., Coulter, E. D., and Dawson, J. H. (1996) Heme-containing oxygenases, *Chem. Rev. 96*, 2841−2847.
27. Ortiz de Montellano, P. R. (1998) Heme oxygenase mechanism: evidence for an electrophilic, ferric peroxide species, *Acc. Chem. Res. 31*, 543−549.
28. Rivera, M., and Zeng, Y. (2005) Heme oxygenase, steering dioxygen activation toward heme hydroxylation, *J. Inorg. Biochem. 99*, 337−354.
29. Rivera, M., Caignan, G. A., Astashkin, A. V., Raitsimring, A. M., Shokhireva, T. K., and Walker, F. A. (2002) Models of the low-spin iron(III) hydroperoxide intermediate of heme oxygenase: magnetic resonance evidence for thermodynamic stabilization of the d_{xy} electronic state at ambient temperatures, *J. Am. Chem. Soc. 124*, 6077−6089.
30. Caignan, G. A., Deshmukh, R., Zeng, Y., Wilks, A., Bunce, R. A., and Rivera, M. (2003) The hydroxide complex of *Pseudomonas aeruginosa* heme oxygenase as a model of the low-spin iron(III) hydroperoxide intermediate in heme catabolism: ^{13}C NMR spectroscopic studies suggest the active participation of the heme in macrocycle hydroxylation, *J. Am. Chem. Soc. 125*, 11842−11852.
31. Zeng, Y., Caignan, G. A., Bunce, R. A., Rodriguez, J. C., Wilks, A., and Rivera, M. (2005) Azide-inhibited bacterial heme oxygenases exhibit an $S = 3/2$ $(d_{xz},d_{yx})^3(d_{xy})^1(d_z^2)^1$ spin state: mechanistic implications for heme oxidation, *J. Am. Chem. Soc. 127*, 9794−9807.
32. Safo, M. K., Gupta, G. P., Watson, C. T., Simonis, U., Walker, F. A., and Scheidt, W. R. (1992) Models of the cytochromes *b*. Low-spin bis-ligated (porphinato)iron(III) complexes with "unusual" molecular structures and NMR, EPR, and Mösbauer spectra, *J. Am. Chem. Soc. 114*, 7066−7075.
33. Evans, D. R., and Reed, C. A. (2000) Reversal of H_2O and OH^- ligand field strength on the magnetochemical series relative to the spectrochemical series. Novel 1-equiv water chemistry of iron(III) tetraphenylporphyrin complexes, *J. Am. Chem. Soc. 122*, 4660−4667.
34. La Mar, G. N., Satterlee, J. D., and De Ropp, J. S. (2000) Nuclear Magnetic resonance of hemoproteins, in *The Porphyrin Handbook 5*, pp 185−297, Academic Press, San Diego, CA.
35. Kumar, D., de Visser, S. P., and Shaik, S. (2005) Theory favors a stepwise mechanism of porphyrin degradation by a ferric hydroperoxide model of the active species of heme oxygenase, *J. Am. Chem. Soc. 127*, 8204−8213.
36. Sugishima, M., Sakamoto, H., Higashimoto, Y., Omata, Y., Hayashi, S., Noguchi, M., and Fukuyama, K. (2002) Crystal structure of rat heme oxygenase-1 in complex with heme bound to azide, *J. Biol. Chem. 277*, 45086−45090.
37. Li, Y., Syvitski, R. T., Auclair, K., Ortiz de Montellano, P. R., and La Mar, G. N. (2003) Solution ^1H, ^{15}N NMR spectroscopic characterization of substrate-bound, cyanide-inhibited human heme oxygenase: water occupation of the distal cavity, *J. Am. Chem. Soc. 125*, 13392−13403.
38. Liu, Y., Zhang, X., Yoshida, T., and La Mar, G. N. (2004) ^1H NMR characterization of the solution active site of substrate-bound, cyanide-inhibited heme oxygenase from *Neisseria meningitidis*: comparison to crystal structures, *Biochemistry 43*, 10112−10126.
39. Liu, Y., Zhang, X., Yoshida, T., and La Mar, G. N. (2005) Solution ^1H NMR characterization of the distal H-bond network and the effective axial field in the resting state, high-spin ferric, substrate-bound complex of heme oxygenase from *N. meningitidis*, *J. Am. Chem. Soc. 127*, 6409−6422.
40. Cheng, H., Westler, W. M., Xia, B., Oh, B.-H., and Markley, J. L. (1995) Protein expression, selective isotopic labeling, and analysis of hyperfine-shifted NMR signals of *Anabaena* 7120 vegetative [2Fe-2S] ferredoxin, *Arch. Biochem. Biophys. 316* 619−634.
41. Delaglio, F., Grzesiek, S., Vuister, G. W., Zhu, W., Pfeifer, J., and Bax, A. (1995) NMRPipe: a multidimensional spectral processing system based on UNIX pipes, *J. Biomol. NMR 6*, 277−293.
42. Goddard, T. D., and Kneller, D. G. Sparky 3, University of California, San Francisco, CA.
43. Wishart, D. S., Bigam, C. G., Yao, J., Abildgaard, F., Dyson, H. J., Oldfield, E., Markley, J. L., and Sykes, B. D. (1995) ^1H, ^{13}C and ^{15}N chemical shift referencing in biomolecular NMR, *J. Biomol. NMR 6*, 135−140.
44. Kay, L. E., Keifer, P., and Saarinen, T. (1992) Pure absorption gradient enhanced heteronuclear single quantum correlation spectroscopy with improved sensitivity, *J. Am. Chem. Soc. 114*, 10663−10665.
45. Simeonov, M., Altuve, A., Massiah, M. A., Wang, A., Eastman, M. A., Benson, D. R., and Rivera, M. (2005) Mitochondrial and microsomal ferric b_5 cytochromes exhibit divergent conformational plasticity in the context of a common fold, *Biochemistry 44*, 9308−9319.
46. Hvidt, A., and Nielsen, S. O. (1966) Hydrogen exchange in proteins, *Adv. Protein Chem. 21*, 288−380.
47. Bai, Y., Milne, J. S., Mayne, L., and Englander, S. W. (1994) Protein stability parameters measured by hydrogen exchange, *Proteins: Struct., Funct., Genet. 20*, 4−14.
48. Unno, M., Matsui, T., Chu, G. C., Couture, M., Yoshida, T., Rousseau, D. L., Olson, J. S., and Ikeda-Saito, M. (2004) Crystal structure of the dioxygen-bound heme oxygenase from *Corynebacterium diphtheriae*: implications for heme oxygenase function, *J. Biol. Chem. 279*, 21055−21061.
49. Schuller, D. J., Wilks, A., Ortiz de Montellano, P. R., and Poulos, T. L. (1999) Crystal structure of human heme oxygenase-1, *Nat. Struct. Biol. 6*, 860−867.
50. Sugishima, M., Omata, Y., Kakuta, Y., Sakamoto, H., Noguchi, M., and Fukuyama, K. (2000) Crystal structure of rat heme oxygenase-1 in complex with heme, *FEBS Lett. 471*, 61−66.
51. Sayers, E. W., and Torchia, D. A. (2001) Use of carbonyl chemical shift to relieve degeneracies in triple-resonance assignment experiments, *J. Magn. Reson. 153*, 246−253.

52. Machonkin, T. E., Westler, W. M., and Markley, J. L. (2004) Strategy for the study of paramagnetic proteins with slow electronic relaxation rates by NMR spectroscopy: application to oxidized human [2Fe-2S] ferredoxin, *J. Am. Chem. Soc. 126*, 5413−5426.
53. Fitzpatrick, T. B., and Malthouse, J. P. G. (1998) A substrate-induced change in the stereospecificity of the serine-hydroxymethyltransferase-catalyzed exchange of the α-protons of amino acids, *Eur. J. Biochem. 252*, 113−117.
54. Cavanagh, J., Fairbrother, W. J., Palmer, A. G., and Skelton, N. J. (1996) Sequential assignments and structure calculations, in *Protein NMR Spectroscopy: Principles and Practice*, 1st ed., pp 532−556, Academic Press, San Diego, CA.
55. La Mar, G. N., and de Ropp, J. S. (1993) NMR methodology for paramagnetic proteins, *Biol. Magn. Reson. 12*, 1−78.
56. Banci, L., Felli, I. C., and Koulougliotis, D. (1998) Identification of slow motions in the reduced recombinant high-potential iron sulfur protein I (HiPiP) from *Ectothiorhodospira halophila* via ^{15}N rotating-frame NMR relaxation measurements, *J. Biomol. NMR 12*, 307−318.
57. Banci, L., Bertini, I., Cavazza, C., Felli, I. C., and Koulougliotis, D. (1998) Probing the backbone dynamics of oxidized and reduced rat microsomal cytochrome b_5 via ^{15}N rotating frame NMR relaxation measurements: biological implications, *Biochemistry 37*, 12320−12330.
58. Zeng, Y., Deshmukh, R., Caignan, G. A., Bunce, R. A., Rivera, M., and Wilks, A. (2004) Mixed regioselectivity in the Arg-177 mutants of *Corynebacterium diphtheriae* heme oxygenase as a consequence of in-plane heme disorder, *Biochemistry 43*, 5222−5238.
59. Zuiderweg, E. R. P. (2002) Mapping protein−protein interactions in solution by NMR spectroscopy, *Biochemistry 41*, 1−7.
60. Wishart, D. S., and Sykes, B. D. (1994) Chemical shifts as a tool for structure determination, *Methods Enzymol. 239*, 363.
61. Lad, L., Wang, J., Li, H., Friedman, J., Bhaskar, B., Ortiz de Montellano, P. R., and Poulos, T. L. (2003) Crystal structures of the ferric, ferrous, and ferrous-NO forms of the Asp40Ala mutant of human heme oxygenase-1: catalytic implications, *J. Mol. Biol. 330*, 527−538.
62. Falzone, J. C., Vu, B. C., Scott, N. L., and Lecomte, J. T. J. (2002) The solution structure of the recombinant hemoglobin from the *Cyanobacterium Synechocystis sp.* PCC 6803 in its hemichrome state, *J. Mol. Biol. 324*, 1015−1029.
63. Wilkens, S. J., Xia, B., Weinhold, F., Markley, J. L., and Westler, W. M. (1998) NMR investigations of *Clostridium pasteurianum* rubredoxin. Origin of hyperfine ^{1}H, ^{2}H, ^{13}C, and ^{15}N NMR chemical shifts in iron−sulfur proteins as determined by comparison of experimental data with hybrid density functional calculations, *J. Am. Chem. Soc. 120*, 4806−4814.
64. Xia, B., Wilkens, S. J., Westler, W. M., and Markley, J. L. (1998) Amplification of one-bond ^{1}H/^{2}H isotope effects on ^{15}N chemical shifts in *Clostridium pasteurianum* rubredoxin by fermi-contact effects through hydrogen bonds, *J. Am. Chem. Soc. 120*, 4893−4894.
65. Jaravine, V. A., Cordier, F., and Grzesiek, S. (2004) Quantification of H/D isotope effects on protein hydrogen-bonds by $^{h3}JH_{NC'}$ and $^{1}J_{NC'}$ couplings and peptide group ^{15}N and ^{13}C′ chemical shifts, *J. Biomol. NMR 29*, 309−318.
66. Wilks, A., Torpey, J., and Ortiz de Montellano, P. R. (1994) Heme oxygenase (HO-1): evidence for electrophilic oxygen addition to the porphyrin ring in the formation of α-meso-hydroxyheme, *J. Biol. Chem. 269*, 29553−29556.
67. Kamachi, T., Shestakov, A. F., Yoshizawa, K. (2004) How heme metabolism occurs in heme oxygenase: computational study of oxygen-donation ability of the oxo and hydroperoxo species, *J. Am. Chem. Soc. 126*, 3672−3673.
68. Davydov, R., Macdonald, I. D. G., Makris, T. M., Sligar, S. G., and Hoffman, B. M. (1999) EPR and ENDOR of catalytic intermediates in cryoreduced native and mutant oxy-cytochromes P450cam: mutation-induced changes in the proton delivery system, *J. Am. Chem. Soc. 121*, 10654−10655.
69. Kamachi, T., and Yoshizawa, K. (2005) Water-assisted mechanism for heme metabolism, *J. Am. Chem. Soc. 127*, 10686−10692.

BI0600188